## Materials and Methods

This work was conducted in accordance with the UK Animals (Scientific Procedures) Act (1986). 10 adult male Lister Hooded rats were chronically implanted in the left and/or right hemisphere with a microdrive (Axona) loaded with four tetrodes (9 rats), or a single Neuropixels(*28*) probe (1 rat). Tetrodes were aimed at the deep layers of the medial entorhinal cortex (mEC, 6 rats: 4.3–4.5 mm lateral to the midline; 0.2–0.5 mm anterior to the sinus; angled forwards in the sagittal plane at 0–10° and 1.5 mm below the pia) and/or CA1 region (6 rats: 2.5 mm lateral to the midline; 4 mm posterior to bregma and 1.4-1.8 mm below the pia). Tetrodes were lowered 100 µm or less per day at the end of each recording session until the first cells of interest were found. The Neuropixels probe was also aimed at the deep layers of mEC (see above). Once implanted the probe provided stable recordings for the duration of experiments (a couple of months) without any adjustments.

Neural activity was recorded while the rats foraged for food in four familiar polygonal enclosures, which varied in shape from a left trapezoid (poly129˚) to a rectangle (poly180˚) and were presented in a random order. The two intermediate shapes were irregular pentagons created by increasing the angle of the west-slanting wall of the trapezoid from 129˚ to either 145˚ or 160˚ (Fig. 1A). Two main requirements were taken into account choosing the shapes of enclosures: they had to provide us with 4 systematic transformations and fit in as much of the 2D pattern as possible while keeping all the transformations distinct.

### Subjects

A total of 10 adult male Lister Hooded rats were used for the experiments. Rats were individually housed in clear plastic cages (68 cm × 44 cm × 48 cm, W × L × H) and were kept on a 12:12 h reversed light: dark cycle (lights on at 10 pm) with controlled temperature (19–23 °C) and humidity (50–70%). The rats weighed 350-450g on the day of surgery. They were maintained on a 90% of body weight food deprivation schedule with the most recent feeding at least 12 h before the recordings. Water was supplied ad libitum.

**Surgery and electrodes**

The rats were anaesthetized with 1–3% of isoflurane in $O_2$ and given a 0.01 mg per 100 g 1:10 diluted i.p. injection of the analgesic Carprieve. Carprieve was given as jelly for three days postop. Nine rats were chronically implanted in the left and/or right hemisphere with a microdrive loaded with eight tetrodes (HM-L coated 90% platinum/10% iridium 17 µm diameter wire). The tetrodes were slightly spread, glued together and cut at the same level. The electrode tips were plated to reduce the impedance to 150–300 kΩ at 1 kHz. Tetrodes were aimed at the deep layers of dorsal medial entorhinal cortex (mEC, 6 rats: 4.3–4.5 mm lateral to the midline; 0.2–0.5 mm anterior to the sinus; angled forwards in the sagittal plane at 0–10° and 1.5 mm below the pia) and CA1 region (6 rats: 2.5 mm lateral to the midline; 4 mm posterior to bregma and 1.4-1.8 mm below the pia). 6 screws were threaded into the skull and the microdrive anchored to them with dental cement. A jeweller's screw fixed to the skull was used as a ground screw.

Additionally, one animal was implanted with a Neuropixels probe. Neuropixels probes are new integrated silicon probes with 960 12 X12 µm recording sites arranged in two columns over a 9.6mm length on a 70 x 20 µm wide shank. Data were amplified, multiplexed and digitized directly on the probe enabling chronic recordings in freely moving rats. The probe was implanted permanently without a microdrive. The probe was glued into a 3D printed plastic holder with a copper mesh cage for protection from external electrical noise. It was aimed at the dorsal medial entorhinal cortex (mEC: 4.5 mm lateral to the midline; 0.3 mm anterior to the sinus; angled forwards in the sagittal plane at 6° and 5 mm below the pia).

After the micro-drive implantation, the rats were given at least 7 days to recover before the experiments were started. The rat implanted with the Neuropixels probe was allowed 24 hours to recover before training to forage and recording commenced.

**Histology and electrode localization**

After completion of the recording sessions the rats were anesthetized with 1–3% of isoflurane in $O_2$ and euthanized using an overdose of sodium pentobarbital followed by transcardial perfusion with saline and 4% of paraformaldehyde (PFA). The brain was cryoprotected in 20% sucrose/PFA solution and sliced into 40 µm parasagittal sections using a cryostat microtome. Sections were mounted and cresyl violet Nissl-stained (tetrode animals) or immunostained for astrocytes with GFAP (Neuropixels probe animal) to allow visualization of the electrode track. Tetrode recording sites were determined by measuring backwards from the deepest point of the track and ensuring that the total length of the electrode track corresponded to the amount of electrode movement as measured from the microdrive screw turns (Fig. S1). 20% shrinkage was allowed for in histology. Neuropixels recording sites were measured from the bottom of the stationary probe. mEC layer II cells were identified as a densely packed strongly stained superficial layer of cells. mEC layer III cells were less intensely stained and less densely packed. mEC layer V cells were intensely stained cells in the pyramidal cell layer adjacent to the lamina dissecans. mEC VI layer were less intensely stained and adjacent to layer V.

**Data collection**

Rats were allowed a recovery period of at least 7 days after surgery (24 hours in case of Neuropixels probe implantation) at which point screening for cells began. Tetrodes were lowered 100 µm or less per day (at 50µm steps) at the end of each recording session until the first cells of interest were found. No screening was required for the animal implanted with a Neuropixels probe. Data were collected using a KC705 FPGA board. Two infrared light emitting diodes (LEDs) of different intensities and separated by 6 cm were fixed on the animal's head in order to track the animal's position and head orientation. The (x, y) coordinates of the LEDs were acquired at 50 Hz by an infrared camera attached to the ceiling above the centre of the environment.

**Single cell isolation from multi-unit recordings**

The experimenter was blind to the cell firing patterns during data collection and cell cluster cutting. Isolation of single units was performed by KlustaKwik(*29*) followed by manual

curation to make sure that noise transients were not included as units and that the same cell was not split into several clusters. Clusters were isolated in a feature space where all possible combinations of pairs of spike amplitudes recorded by the four tetrodes were plotted against each other. Unit isolation was further refined by taking into account additional properties of spike waveforms such as the existence of positive pre-potentials. The clusters were included into the analysis if: the cell refractory period was >2 ms and the cell fired at least 150 spikes in at least two enclosures. The clusters were assigned to the same cell on different trials if: the tetrode had not been moved between trials; there was minimal change in spike waveforms; the position of the target cluster and neighbouring clusters remained similar in feature space. In the case of newly appearing fields, these were cut separately and their waveforms compared to the entire cluster to make sure that they were identical. Finally, only cells with well-defined fields were included for future analysis. Neuropixels probe data were isolated using Kilosort(*30*). Isolated single units were manually curated using PHY(*31*) following the criteria described above.

**Training procedures and testing environments**

Cells were recorded in four different wooden polygonal enclosures varying in shape from a left trapezoid (called poly129˚ to reflect the angle between the base and the apex) to a rectangle (1.8m x 1.0m) called poly180° with two intermediate shapes which were irregular pentagons created by increasing the angle of the west-slanting wall of the trapezoid from 129˚ to either 145˚ (poly145˚) or 160˚ (poly160˚) (Fig. 1A). All enclosures were made from the same four 1.8m x 50 cm boards stood on edge. The poly 180° rectangle measured 1.8m x 1.0m whereas the other polygons measured: 1.8m x 1.0m x 1.0m x 1.3m (poly 129°); 1.8m x 1.0m x 1.0m x 1.0m x 0.45m (poly 145°); 1.8m x 1.0m x 1.0m x0.87m x 0.71m (poly 160°). Each recording session usually consisted of two to four 30 min long trials in different enclosures presented in a random order. Occasionally the same randomly chosen enclosure was presented twice in a session to check the stability of the firing pattern when no change in geometry occurred. The animal had ~10–15 min breaks between trials during which they sat on a small open platform in the same room. The animals were not disoriented between the trials. All enclosures were centred at the same position in the room below the tracking camera and the enclosure reconfigurations were

visible to the animal. The room was well illuminated with multiple cues positioned around the recording enclosures including one large well-illuminated white card (1.13 m × 0.83 m) at the west side of the environment. Initial cell screening was carried out in the poly129˚ enclosure (except for the rat implanted with Neuropixels probe who was initially trained in a rectangle) for ~7 days or until the first spatially modulated cells were recorded and then the training in other enclosures would commence to ensure that all enclosures were familiar to the animal (at least 5 exposures) prior to recordings.

**Firing rate maps**

A locational firing rate map was constructed by dividing the number of spikes fired in a given part of the environment by the time spent there. Position data and spike counts were sorted into 2.6 cm × 2.6 cm spatial bins. Unsmoothed firing rate maps were obtained by dividing the spike count in each bin by the dwell time in that bin. The firing rate map was smoothed by applying adaptive smoothing as previously described in(*13*). Colour bars represent firing rate in deciles of the range of firing rates (top 10% in red, bottom 10% in blue). Unvisited bins are shown in white.

Directional firing rate was estimated by dividing spike counts and dwell times into 3$^{o}$ bins. Boxcar smoothing of 5 bins (15 $^{o}$) was applied to spike and dwell time maps before dividing them. The preferred direction was defined as a direction with the largest firing rate with the exception of three cases in which it was obviously incorrectly skewed by outliers. In these case the direction was calculated as a vector sum from all the points in the polar rate map.

**Cell classification**

Grid cells were defined as cells with a gridness score >0.27 in at least one enclosure and head direction cells were defined as cells with a Rayleigh vector >0.3 as described in(*15*). Border cells were active only close to one of the walls or two of the adjacent walls.

**Evaluating field shift**

We evaluated the shift in a field position by looking at the change in field centre coordinates in different enclosures within a session for each individual cell. All possible permutations of pairs of transformations were included preserving their chronological order. For example, the data from a session with three trials, A, B, C (in that order) would be used to construct three ("A->B", "B->C", "A->C") vector maps. To identify the individual fields of a spatially periodic cell, logarithmic rate maps were used. Each rate map was normalized to have the values from zero to one and a threshold of 0.7 was applied. The individual regions with at least eight adjacent above-threshold bins were defined as fields. To ensure correct assignment of the field centres (e.g. detecting weak fields and separating close fields so they are not merged) a manual check was subsequently performed on each rate map. Only a small proportion of field assignments had to be adjusted. The bin with the maximum firing rate was defined as the centre of the field (unless it was a clear outlier on the edge of the field in which case a centre of mass was chosen as the field centre). The pairing of corresponding fields from different rate maps was based on their proximity compared to the proximity of other fields. The overall average vector field was calculated by taking the mean field shift in a 5x5 bin area (corresponding to 13x13cm$^2$ region) from all grid cells (or place cells). The tail of the resultant vector was shown in the centre of the corresponding bin.

**The range of field movement**

We used the vector fields (see 'Evaluating field shift') to estimate the range and maximum field shifts. The threshold of significant shift was defined as the intrinsic shift due to tracking resolution, differences in animal positional sampling and other uncontrolled variations between experimental conditions and was calculated as the average shift of all available vector field maps

in transformations with no change to the enclosure geometry: 6.8 cm for place cells (46 transformations; 4 rats) and 5.7 cm for grid cells (9 trials; 3 rats). It is also comparable to previously reported position measurement error(*32*).

**Directions of field movement**

We used the vector fields (see 'Evaluating field shift') to calculate the directions in which fields moved. Only fields with significant shifts were included. To evaluate whether the directionality of field movement correlated with the angle of the moving wall (i.e. was perpendicular to it) or was more biased towards vertical or horizontal movement we calculated the average distribution of these directions in all transitions to the poly129˚ enclosure (poly145˚->poly129˚; poly160˚->poly129˚; poly180˚->poly129˚) as well as all transitions to the poly145˚ enclosure (poly160˚->poly145˚; poly180˚->poly145˚) in expanding transformations and transitions to the poly160˚ (poly129˚->poly160˚; poly145˚->poly160˚) and to the rectangle (poly129˚->poly180˚; poly145˚->poly180˚; poly160˚->poly180˚) in all contracting transformations.

**Simultaneous changes in grid cells and place cells**

We investigated the correlation between the individual field shifts of simultaneously recorded grid cells and place cells. In this analysis we included the data from transformations poly129˚ to a rectangle (and vice versa) and poly145˚ to rectangle (and vice versa) since the field shifts in these transformations were most pronounced. A vector field was generated for each grid cell pair by taking the mean field shifts in a 39x39 $cm^2$ area. We have defined a 'direction similarity matrix' and a 'magnitude similarity matrix' to evaluate how similar the directions and amounts in which the co-localised fields moved. The GC-GC direction similarity for each bin was calculated as:

$$GC-GC\ direction\ similarity(x_{bin},y_{bin}) = \frac{\sum_{i,j(i\neq j)}^{N_{GCpairs}} \cos(\alpha_i - \alpha_j)}{N_{GCpairs}}$$

where $\alpha_{i,j}$ directions in which grid cell *'i'* and grid cell *'j'* shifted; ($x_{bin}$,$y_{bin}$) – their starting position; $N_{GCpairs}$ – the number of co-recorded pairs of grid cells in this position. In case of fields with aligned directions of movements, the direction similarity is equal to '1'. If the fields shift in perpendicular directions (or random directions), their similarity index is equal to zero; whereas if they shift in opposite directions, the similarity is equal to '-1'.

The PC-GC direction similarity for each bin was calculated as:

$$PC - GC\ direction\ similarity(x_{bin}, y_{bin}) = \frac{\sum_{i,j}^{N \times M} \cos(\alpha_i - \alpha_j)}{N \times M}$$

where *N* and *M* are the numbers of grid and place cell respectively; $\alpha_i$ and $\alpha_j$ are the directions of grid field and place filed shifts respectively.

The similarity between GC-GC amounts of shift for every bin of the 'magnitude similarity matrix' was calculated as:

$$GC - GC\ magnitude\ similarity(x_{bin}, y_{bin}) = \frac{\sum_{i,j(i \neq j)}^{N_{GCpairs}} \left(1 - \frac{|A_i - A_j|}{\frac{A_i + A_j}{2}}\right)}{N_{GCpairs}}$$

where $A_i$ and $A_j$ are the amounts of shift of co-localized fields of grid cell *'i'* and grid cell *'j'* respectively; $N_{GCpairs}$ – the number of co-recorded pairs of grid cells. In case field shifts of identical distances, the magnitude similarity is equal to '1' and it reduces towards '-1' with large disparities.

The PC-GC magnitude similarity for each bin was calculated as:

$$GC - PC\ magnitude\ similarity(x_{bin}, y_{bin}) = \frac{\sum_{i,j}^{N \times M} \left(1 - \frac{|A_i - A_j|}{\frac{A_i + A_j}{2}}\right)}{N \times M}$$

where *N* and *M* are the numbers of grid and place cells respectively; $A_i$ and $A_j$ are the amounts of shift of co-localized fields of grid cell *'i'* and place cell *'j'* respectively.

We evaluated the significance of similarity values by randomly shuffling the starting positions of the vector fields (binned into 3x5 matrix) of all co-recorded cell pairs and calculated their direction and similarity matrices. In each surrogate the similarity expected by chance was equal to the maximum value of the surrogate map. All cell pairs were considered and the shuffling was carried out 200 times. The 95$^{th}$ percentile was used as a threshold criteria. The bins with similarity values above the threshold corresponded to locations where fields of co-recorded grid cells (place cells) moved in register with each other.

**Modelling short range border cell effects on grid cells**

Only rectangle-to-poly129˚ transformations were used to model the border cell effect on grid cell firing patterns. All the first trial maps (rectangular enclosure) were transformed in the following way: for the west (south) border cell effect the grid cell field within 30 cm from the border was shifted to align to the new position of the wall overriding the previous fields in this area and not affecting the more distant fields. Field shifts were estimated as previously described in 'Evaluating field shift'. The maximum field shift was used to assess the relationship between the grid scale and the field shift. The cross-correlation between the simulated and the second rate map was used to evaluate how well this model captured the real data. We also repeated the same procedure with 50 cm and 70 cm ranges of border effects which did not change the initial results.

Border cells with fields adjacent to the slanting wall changed their receptive fields to continue to abut it. Our data showed that border cells (26 mEC border cells, 3 rats) active along

the west and south walls often extended their firing onto the slanting wall whereas those firing at the stationary north or east walls remained unchanged (Fig. S8A).

This simple model was unable to account for our results. We looked at the largest transformation (rectangle to poly129˚ (Fig. S8B-D)) and found that the average cross-correlation coefficients between the west side grid pattern of the first and the second experimental enclosures, and between the first experimental and the simulated enclosure were not significantly different (Fig. S8C, 0.48$\pm$0.02; 0.44$\pm$0.02 respectively; p=0.33, multi-comparison with Bonferroni correction). Both were significantly lower than those of the east side (0.73$\pm$0.01, $p=4*10^{-9}$, multi-comparison with Bonferroni correction) suggesting that the model does not perform better than the assumption of a stable grid, which in turn can be ruled out given the difference in cross-correlation between the east and west sides. Importantly, this model predicts a significant correlation between the grid scale and the field shift (Fig. S8) which was not observed in our experimental data (Fig. 3B).

**Measuring mean grid scale as well as its horizontal and vertical components**

The mean grid scale was measured from the local spatial auto-correlogram as previously described(*13*) taking the mean distance between the centre and three surrounding peaks. In case of spatially periodic non-grid cells the distance corresponded to the mean distance between the centre to the closest local spatial peaks (1-3 peaks). The horizontal grid scale was equal to the average distance between the centre and local peaks occurring between angles of -44 and 45 and between 136 and 225 degrees whereas the vertical scale was equal to the average distance between the centre and local peaks at 46-135 and 226-315 degrees.

**Grid homogeneity test along the long axis of the enclosure**

For simplicity, in our simulations we used a vertical periodic band to model our observations (Fig. S9). Its spatial frequency in the first enclosure was set equal to the experimentally observed average grid scale and in the second was randomly rescaled by <$\pm$10%

('+' and '-' for expanding and contracting transformations respectively) with the offset fixed to the east wall. This simple model captured several of the key experimental observations: (1) field shifts were larger closer to the slanting wall, (2) their maximum magnitudes were similar to experimentally observed ones (<20 cm), and (3) the shifts were comparable for all grid scales within a given range. However, this model predicts that the largest field shifts should be observed at the top west corner of the enclosure, whereas they were most prominent in the bottom west region, reflecting the strong influence of the slanting wall and suggesting that grid rescaling may not have been uniform.

To test how homogeneous the rescaling was, we examined how the structure changed as we gradually exposed more of the western part of the field. We started with a $\Delta x$=50 cm x 1 m area abutting the east wall in the first enclosure and compared it with a $\Delta x \pm \delta$ area of the second enclosure, where $\delta$ varied from -13 to 13 cm in 2.6 cm steps. Each of the latter were rescaled back to $\Delta x$ to match the sizes of the two exposed areas for comparison. Optimal rescaling corresponded to the largest cross-correlation coefficient and was calculated as

$$GC\ rescaling(\Delta x) = -\frac{\delta}{\Delta x}$$

The exposed area of the first enclosure was gradually expanded along the long axis of the enclosure towards the slanted west wall by incrementally increasing $\Delta x$ in 10.4 cm steps to a maximum of 161 cm, repeating the same optimal rescaling procedure.

The periodic bands in the second simulated enclosure were either uniformly or non-uniformly rescaled in the x dimension and anchored to the east wall. We also repeated this procedure on the same dataset but starting from the west wall instead.

Uniform grid scale changes should yield a constant rescaling along the entire length of the enclosure (Fig. 2E). In contrast, we found that in the majority of expanding and contracting transformations the rescaling varied across the enclosure (Fig. 2C) suggesting a non-uniform grid

scale change (Fig. 2D). The average correlation coefficients were significantly higher between the first rate map and the rescaled second rate map compared to the non-rescaled second rate map (0.68±0.01 vs. 0.64±0.01 respectively; p=0.00004; $t_{20}$=5.19, two-sample t-test). The observed rescaling profile was steeper than that predicted by a uniform grid rescaling (with rescaling equal to the ratio between the mean grid scale in the second and the first enclosures) and showed a significantly higher mean correlation coefficient (0.68±0.01 vs. 0.59±0.01; $p=4*10^{-11}$; $t_{20}$=12.96, two-sample t-test).

Our rescaling model assumed grid offset fixed to the stable east wall and resulted in lower cross-correlations coefficients if the same analysis was with a grid anchored to the west wall: mean correlation coefficients 0.68±0.01 vs. 0.58±0.01 respectively ($p=9*10^{-11}$, $t_{20}$=12.33, two-sample t-test). Thus, the grid was primarily fixed to stable east boundaries even though border cell signals were defined along all the available boundaries.

**Evaluating the effects of directional sampling variability on firing rate maps in grid cells and place cells**

We evaluated how well the changes in firing patterns could be explained by the difference in the animal's running direction. The rate maps were recalculated after filtering the animal's running direction as it was running eastwards (0±45 deg), northwards (90±45 deg), westwards (180±45 deg) and southwards (270±45 deg). Directionally balanced rate maps of the first and the second enclosures were obtained so that each filtered direction only included bins visited in both enclosures in a given direction. The balanced unsmoothed maps were combined again to obtain the overall directionally balanced rate map. We calculated the cross-correlation coefficients of the left (and right) half of the first enclosure and the corresponding half of the second enclosure (the unvisited bins of the larger enclosure were not included into calculations). The analysis was done on both directionally balanced and normal rate maps: only (filtered) trials with >100 spikes were included (having zero threshold did not change the results). Also the number of spikes were calculated for each running direction.

No significant difference was observed between these two sampling modes (Fig. S6). Namely, we found that the cross-correlations between the left sides of the first and the second rate maps were significantly lower compared to the right sides in both down-sampled and normal rate maps (balanced right and left sides: 0.58±0.04 vs. 0.72±0.03, $t_{12}$=-2.8, p=0.02; normal right and left sides: 0.56±0.04 vs. 0.70±0.04, $t_{12}$=-2.7, p=0.02, two-sample t-test), but there was no difference between the two on either left or right sides (left: $t_{12}$=0.23, p=0.82; right: $t_{12}$=0.36, p=0.72, two-sample t-test).

For one animal with the largest number of recorded grid cells (R2405) we selected the centres of fields anew in directionally balanced rate maps and recalculated the vector fields as previously described. We compared the new vector field with the one previously obtained (with the unbalanced directional sampling) and found no discernible difference between them (Fig. S6).

In addition , the cross correlations and normalised spike numbers defined as $\frac{n_{dir2}-n_{dir1}}{n_{dir2}+n_{dir1}}$ were calculated between rate maps filtered by different running directions taking into account all possible pairs: north-south; east-west; north-west; north-east, south-west, and south-east to investigate if there was a difference between these measures. Again, we found no significant differences in cross correlation coefficients or the number of spikes of directionally filtered rate maps (Fig. S7; the cross-correlation coefficients: F(5, 36)=1.94, p=0.11; the normalized number of spikes: F(5, 36)=0.54, p=0.74; the number of spikes: F(3, 24)=0.49; p=0.69; one-way ANOVA).

The analysis was carried out for each animal for grid cells and place cells separately.

**Decoding procedure**

Single step Bayesian decoding was used to estimate a rat's position in each time bin(*33*). The probability of rat's position was calculated by applying Bayes' rule:

$$P(x|\boldsymbol{n}) = \frac{P(\boldsymbol{n}|x)P(x)}{P(\boldsymbol{n})}$$

Here P(**n**|x) is the probability for the grid cell ensemble N to fire **n** spikes, P(x) is the probability of an animal being in a particular location during the trial and P(**n**) is the normalization factor. The posterior probability of locations expressed through the activity of grid cell ensemble:

$$P(x|\boldsymbol{n}) = \frac{P(x)}{P(\boldsymbol{n})} \cdot \prod \frac{\Delta t f_i(x)^{n_i}}{n_i!} \exp[-\Delta t f_i(x)]$$

Here $\Delta t$ is the time bin for the sliding window, $f_i(x)$ is the mean firing rate for *i*th grid cell and $n_i$ is the number of spikes in the particular time bin for the *i*th grid cell. The maximum of this function corresponds to the reconstructed position. The time bin was set to 1s and both reconstructed position and decoding error, defined as linear difference between reconstructed and measured positions, were calculated for each bin. For theoretical convenience grid cells were treated as independent Poisson neurons similar to (*33*).

**Simulated data:** a set of grid cells from two different grid modules (50cm and 80cm wavelengths, consistent with our recorded data) was simulated using random offsets and the same grid orientation. Grid field sizes and maximum firing rates were matched to the recorded data. Two additional grid cell sets were generated from this set by applying two types of grid transformations. The first set had a non-linear (quadratic) GC pattern transformation where all grid cells were on average rescaled by -10% ('-' indicates that the scale was reduced; the magnitude of rescaling was gradually decreasing along x axis as previously described; all grid cells were resized in sync). Grid cells of the second set were randomly rescaled (uncoupled) by – (1-19)% (same average effect size but different magnitudes of individual transformations). The resizing factor of -10% was selected to match a rectangle to poly129° transformation. For each cell in both sets, a spike train was generated by a Poisson process. The running path was taken from our measured data set. The left (west) most 30 cm of the environment was not included in

the calculation of position reconstruction error shown in Fig. 3E due to the grid cell pattern rescaling rendering the error in this region meaningless (Fig. S10B).

**Results:** the decoding of the rat's position from a trial with 50 simultaneously recorded grid cells in a rectangular environment was performed. The mean error of the reconstructed position was 16.0 cm. This is comparable with the simulated data where decoding error for 50 grid cells was 14.1±0.8 cm.

Next we looked at the decoding error for a transformation where all simulated grid cells rescaled in register compared to the situation where individual grid cell transformations were uncoupled. Posterior probability of position for each rescaled ensemble was calculated using respective simulated spike trains and firing rates from grid cell data recorded in a rectangle. We found that the position reconstruction error was 50% higher when grid cells transformations were uncoupled even if the average rescaling was the same (Fig. 3E). The prediction error for the reconstructed position consisted of two parts: (1) the stochastic decoding error caused by behavioural sampling and recording limitations and (2) the systematic decoding error determined by the amount of grid rescaling, which could be compensated if the average effect size was known (Fig. 3F).

**Supplementary Figure Legends**

**Fig. S1**

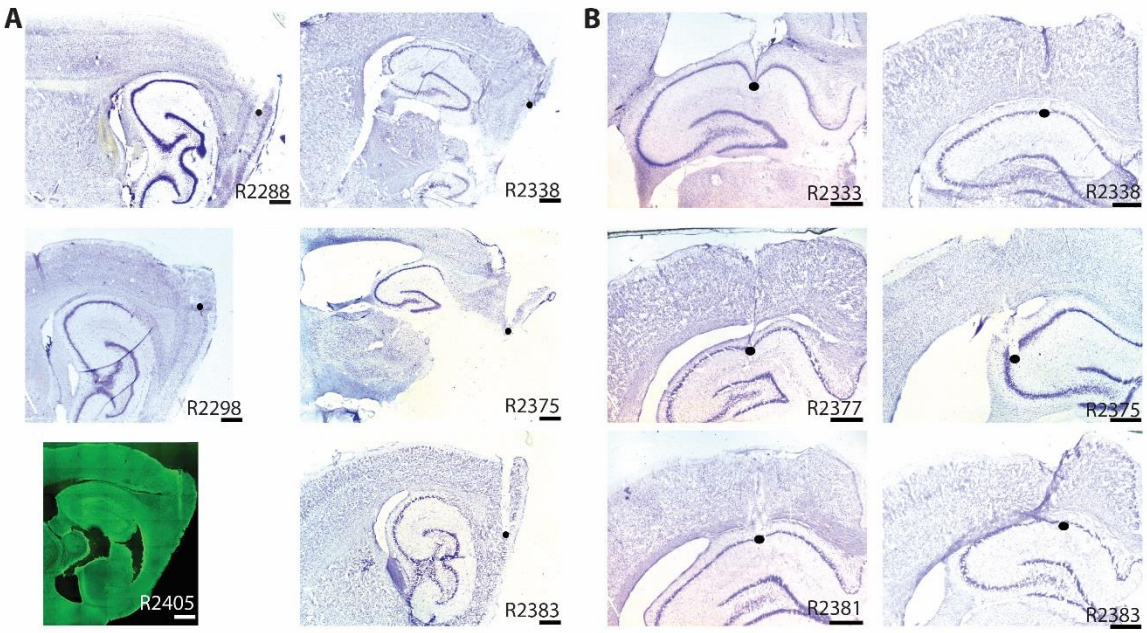


**Sagittal Nissl-stained brain sections showing the recording locations in mEC and CA1**. (**A**) mEC recordings. (**B**) CA1 recordings. Bottom right: rat ID. Bar: 1 mm. R2405 section was immune-stained for GFAP (astrocytes) and shows the position of Neuropixels probe.

**Fig. S2**

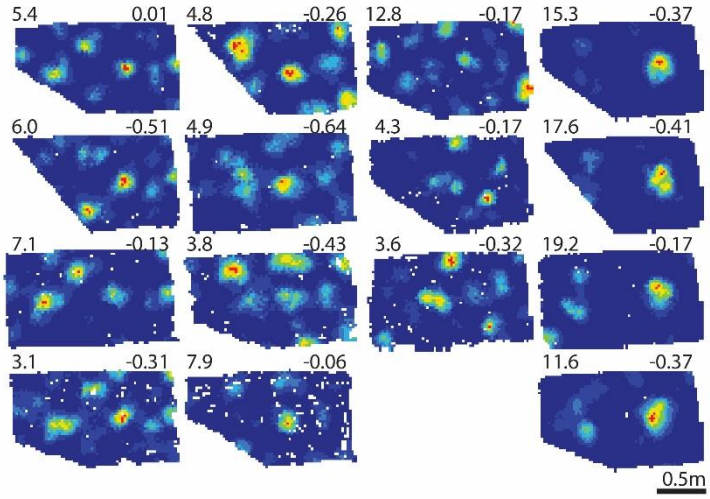


**Spatially periodic non-hexagonal cells.** Typical examples of spatially periodic non-grids. Different columns represent different cells recorded in four rats. Top left: peak firing rate; top right: gridness score. Note that the fields close to the slanting wall move while the distant ones remain fixed.

**Fig. S3**

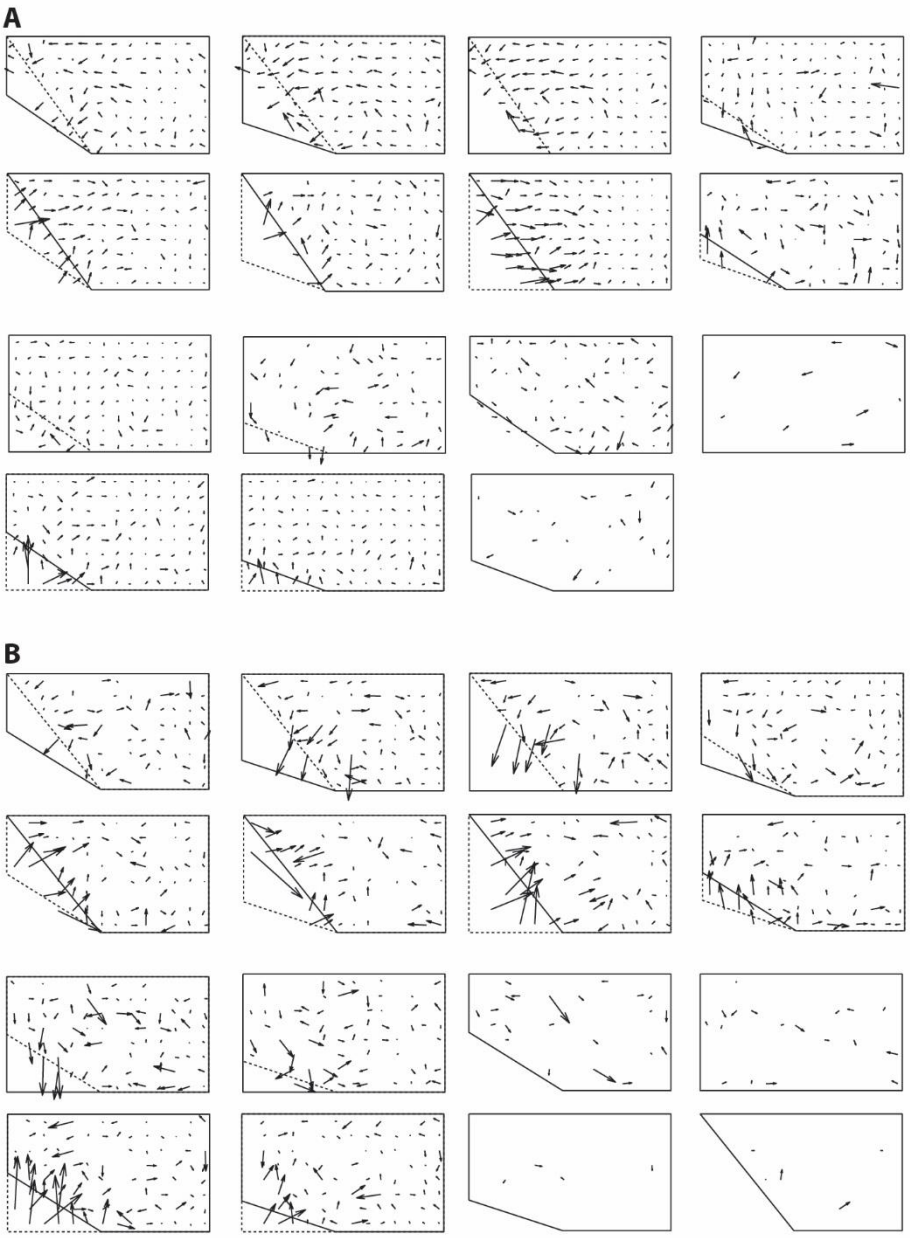


**Grid and place field shifts with gradual systematic changes to enclosure shape**. **(A-B)** mean vector fields of all the recorded grid cells (A) and place cells (B) indicating average field shifts between pairs of successive (but not necessarily immediately following each other) geometrical enclosures: the vector tail specifies field position in the first enclosure. The first and the second enclosures shown in dashed and solid lines respectively.

**Fig. S4**

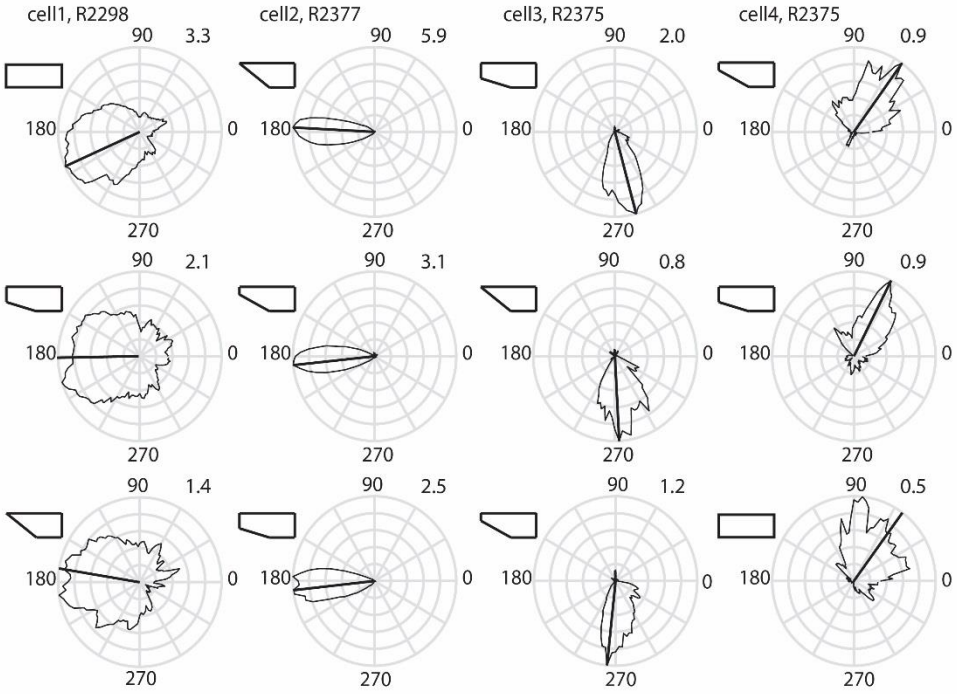


**Four recorded head direction cells from three different rats (R2298, R2377, R2375)**. Polar plots of four head direction cells recorded in three different enclosures shown in the upper left corner. Preferred head direction (HD) indicated with a solid line. Trials presented in their recording order.

**Fig. S5**

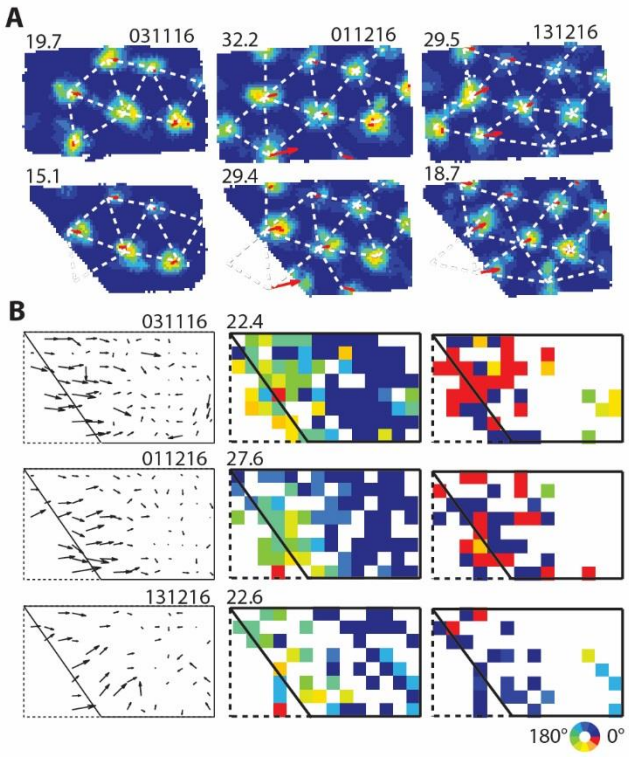


**Change of grid field positions across days.** (**A**) examples of three grid cells (R2405) shown in different columns recorded in rectangular and poly129˚ enclosures on three different dates spanning 39 days. Top left: firing rate. White dashed line defines the grid structure from the rectangle also overlaid on the poly129˚ enclosure. Arrows indicate field shifts. (**B**) vector fields indicating field shifts on three different days (left column). Magnitudes and directions of field shifts shown in middle and right columns respectively. Top right corner: date of recording. Top left corner: maximum shift in cm. Note the similarity over time.

**Fig. S6**

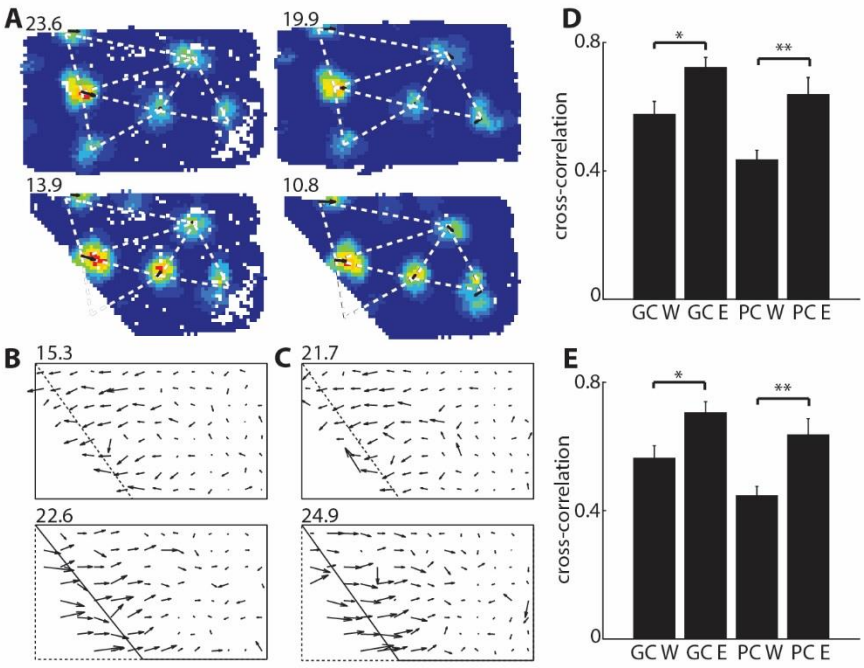


**Field shifts between rate maps of comparable directional sampling.** (**A**) typical grid cell in first rectangular (top) and second poly129˚ enclosures (bottom) during directionally balanced (left) and normal enclosure (right) sampling. Top left: peak firing rate. (**B** and **C**) vector fields from rate maps with directionally balanced (B) and normal (C) enclosure sampling. Dashed and solid lines: the first and the second enclosures respectively. Top left: the largest field shift in cm. (**D** and **E**) cross-correlations between west (W) and east (E) parts of first and second enclosures for grid cells (GC) and place cells (PC) in directionally balanced enclosure sampling (D) and normal sampling (E). The cross-correlation of rate maps with balanced directional sampling was comparable to that with normal sampling.

**Fig. S7**

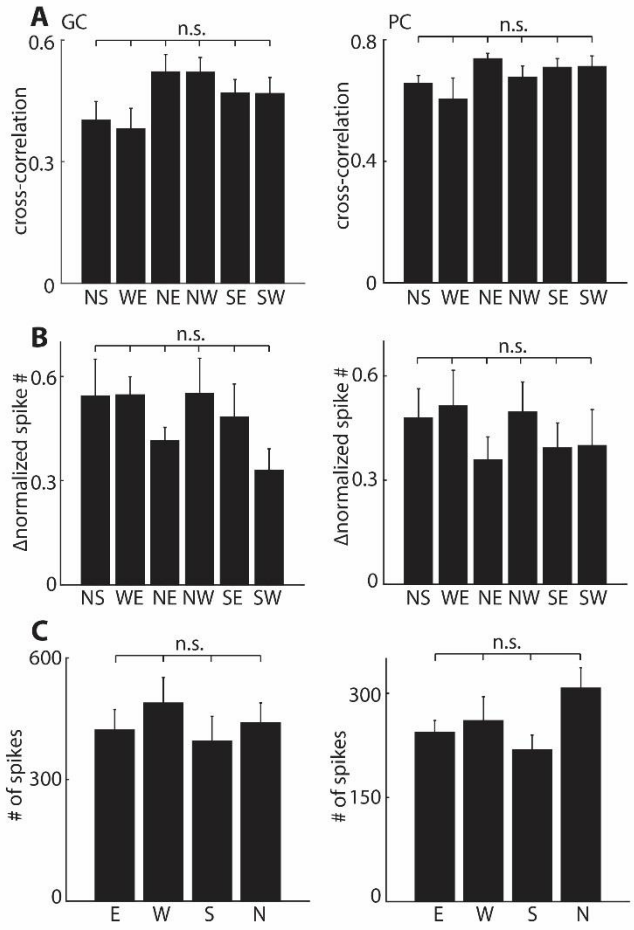


**The firing patterns of both grid cells and place cells are independent of animal's running direction.** (**A**) average cross-correlation coefficients between grid (left) and place (right) cell firing patterns as the animal ran in six different directions. NS, WE, NE, NW, SE, SW specify north-east, west-east, north-east, north-west, south-east, south-west respectively. n.s.: statistically non-significant; one way ANOVA: $F_{GC}(5, 36)=1.94$, $p_{GC}=0.11$; $F_{PC}(5, 30)=1.46$, $p_{PC}=0.23$. (**B**) average normalized spike number differences of grid (left) and place (right) cell as the animal ran in different directions: $F_{GC}(5, 36)=0.54$, $p_{GC}=0.74$; $F_{PC}(5, 30)=1.25$, $p_{PC}=0.31$. (**C**) grid (left) and place (right) cell average spike numbers fired as the animal ran in four different directions; E, W, S, N: east, west, south and north respectively: $F_{GC}(3, 24)=0.49$, $p_{GC}=0.69$; $F_{PC}(3, 20)=1.99$, $p_{PC}=0.15$.

**Fig. S8**

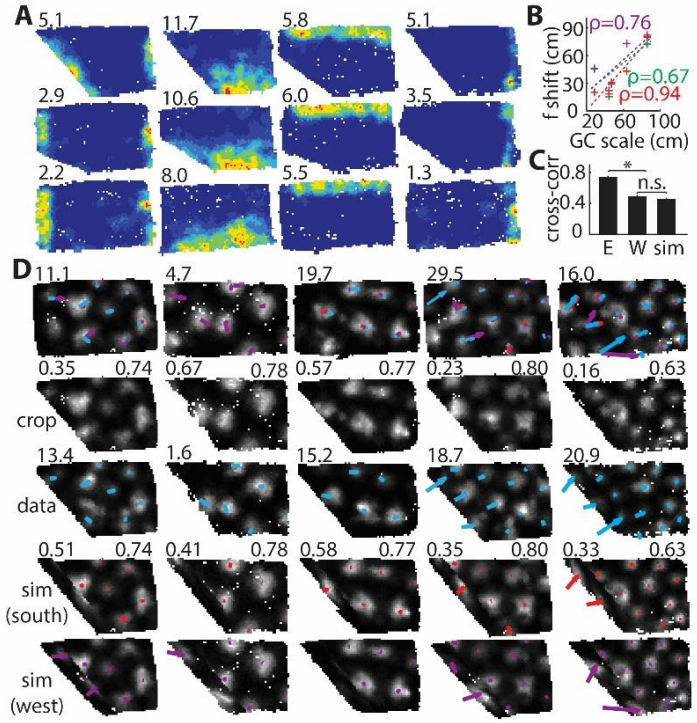


**Modeling direct effect of borders on grid cells.** (**A**) example border cells recorded simultaneously with grid cells. Border cells (R2298 and R2375) with fields abutting the slanting wall (2 left columns) move with the wall (or disappear: second column, top row); border cells away from the slanting wall remain constant (2 right columns). (**B**) simulations of direct BC effect predict that the shift should be proportional to the grid scale: red, violet and green correspond to effects from south, west or combined respectively. (**C**) cross-correlations between the east (E) sides of manipulated grid cell rate maps is significantly larger than the west side (W). Cross-correlation coefficients between the west sides of the first and the second and the first and simulated rate maps ('sim') are not significantly different. (**D**) example grid cells (R2375 and R2405) of different scales with new field positions approximated by direct effects from border cells. Top and third rows: peak firing rates. Second and fourth rows: cross-correlation coefficients between west (top left corner) and east (top right corner) sides of the first and the second (second row) and the first and simulated rate maps (fourth row). 'crop' corresponds to rate maps in the first row above cropped to the same size as rate maps in the row below ('data').

**Fig. S9**

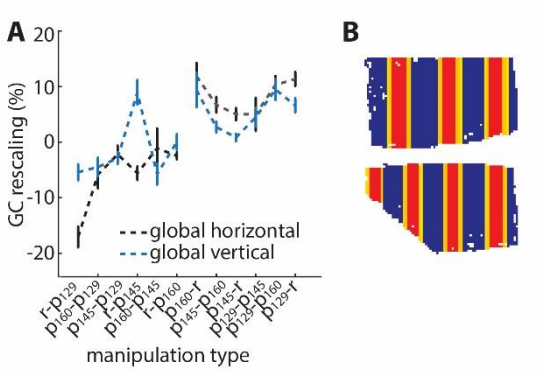


**The rescaling tended to be larger along the long horizontal axis of the enclosure compared to the vertical axis.** (**A**) average rescaling during different transformation types in horizontal and vertical axis. (**B**) example of vertical periodic bands used to model non-uniform rescaling.

**Fig. S10**

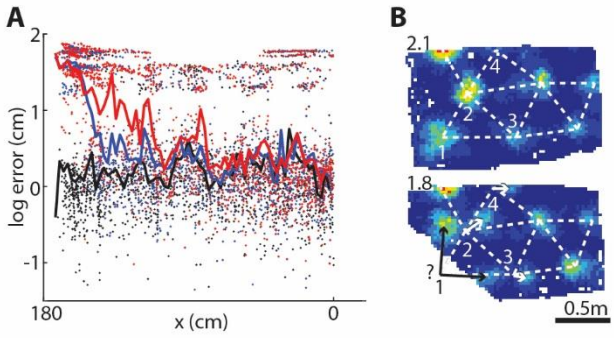


**The position decoding error along x axis.** (**A**) position decoding error for in register (blue) vs uncoupled grids (red). Black: baseline. Dots represent position decoding errors at individual time bins and solid lines correspond to their averages. Note sharp increase of the decoding error within ~30 cm distances from the west slanting wall for both transformations due to newly appearing fields in rescaled grid cells: here the decoding breaks down since initial rate maps do not cover this area. '0' coordinate corresponds to the east wall. (**B**) an example of a grid cell with newly appearing fields. Dashed line outlines grid structure in the rectangle. Top left: peak firing rates.

**Fig. 11**

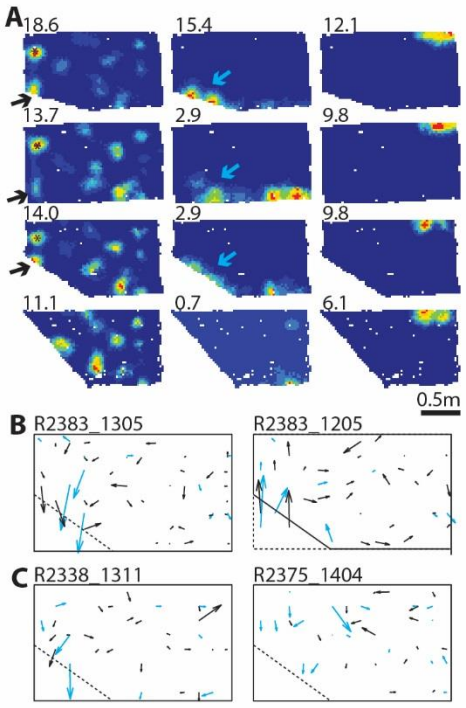


**Changes in grid and place fields were different albeit sometimes showing similar trends**. (**A**) example of simultaneously recorded grid cell and two place cells. Grid Field (left column) and place cell field (middle column) close to the slanting wall shift with the wall; Place field distant from the wall (right column) remains unchanged. Blue (place) and black (grid) arrows represent moving fields. (**B**) two vector fields from simultaneously recorded grid cells (black) and place cells (blue) in expanding (left) and contracting (right) transformations show similar trends. The correlations between poly160˚ to poly129˚ shift reaching 0.70±0.18 (3 days, p=0.02, binomial test), and the rectangle to poly145˚ at 0.35±0.17 (7 days, p=0.056). (**C**) two other examples of the same expanding transformation in two different rats showing less similarity. Rats: R2383, R2338, R2375.

**References**


1. J. O'Keefe, J. Dostrovsky, The hippocampus as a spatial map. Preliminary evidence from unit activity in the freely-moving rat. *Brain Res.* **34**, 171–175 (1971). doi:10.1016/0006-8993(71)90358-1 Medline

2. J. S. Taube, R. U. Muller, J. B. Ranck Jr., Head-direction cells recorded from the postsubiculum in freely moving rats. I. Description and quantitative analysis. *J. Neurosci.* **10**, 420–435 (1990). Medline

3. T. Solstad, C. N. Boccara, E. Kropff, M.-B. Moser, E. I. Moser, Representation of geometric borders in the entorhinal cortex. *Science* **322**, 1865–1868 (2008). doi:10.1126/science.1166466 Medline

4. C. Lever, S. Burton, A. Jeewajee, J. O'Keefe, N. Burgess, Boundary vector cells in the subiculum of the hippocampal formation. *J. Neurosci.* **29**, 9771–9777 (2009). doi:10.1523/JNEUROSCI.1319-09.2009 Medline

5. F. Savelli, D. Yoganarasimha, J. J. Knierim, Influence of boundary removal on the spatial representations of the medial entorhinal cortex. *Hippocampus* **18**, 1270–1282 (2008). doi:10.1002/hipo.20511 Medline

6. T. Hafting, M. Fyhn, S. Molden, M.-B. Moser, E. I. Moser, Microstructure of a spatial map in the entorhinal cortex. *Nature* **436**, 801–806 (2005). doi:10.1038/nature03721 Medline

7. J. O'Keefe, L. Nadel, *The Hippocampus as a Cognitive Map* (Oxford Univ. Press, 1978).

8. E. I. Moser, M.-B. Moser, A metric for space. *Hippocampus* **18**, 1142–1156 (2008). doi:10.1002/hipo.20483 Medline

9. B. L. McNaughton, F. P. Battaglia, O. Jensen, E. I. Moser, M.-B. Moser, Path integration and the neural basis of the 'cognitive map'. *Nat. Rev. Neurosci.* **7**, 663–678 (2006). doi:10.1038/nrn1932 Medline

10. M. C. Fuhs, D. S. Touretzky, A spin glass model of path integration in rat medial entorhinal cortex. *J. Neurosci.* **26**, 4266–4276 (2006). doi:10.1523/JNEUROSCI.4353-05.2006 Medline

11. N. Burgess, C. Barry, J. O'Keefe, An oscillatory interference model of grid cell firing. *Hippocampus* **17**, 801–812 (2007). doi:10.1002/hipo.20327 Medline

12. M. E. Hasselmo, Grid cell mechanisms and function: Contributions of entorhinal persistent spiking and phase resetting. *Hippocampus* **18**, 1213–1229 (2008). doi:10.1002/hipo.20512 Medline

13. J. Krupic, M. Bauza, S. Burton, C. Barry, J. O'Keefe, Grid cell symmetry is shaped by environmental geometry. *Nature* **518**, 232–235 (2015). doi:10.1038/nature14153 Medline

14. T. Stensola, H. Stensola, M.-B. Moser, E. I. Moser, Shearing-induced asymmetry in entorhinal grid cells. *Nature* **518**, 207–212 (2015). doi:10.1038/nature14151 Medline

15. J. Krupic, N. Burgess, J. O'Keefe, Neural representations of location composed of spatially periodic bands. *Science* **337**, 853–857 (2012). doi:10.1126/science.1222403 Medline

16. H. Stensola, T. Stensola, T. Solstad, K. Frøland, M.-B. Moser, E. I. Moser, The entorhinal grid map is discretized. *Nature* **492**, 72–78 (2012). doi:10.1038/nature11649 Medline

17. J. Krupic, M. Bauza, S. Burton, C. Lever, J. O'Keefe, How environment geometry affects grid cell symmetry and what we can learn from it. *Philos. Trans. R. Soc. Lond. B Biol. Sci.* **369**, 20130188 (2013). doi:10.1098/rstb.2013.0188 Medline

18. J. J. Knierim, H. S. Kudrimoti, B. L. McNaughton, Place cells, head direction cells, and the learning of landmark stability. *J. Neurosci.* **15**, 1648–1659 (1995). Medline

19. K. J. Jeffery, Learning of landmark stability and instability by hippocampal place cells. *Neuropharmacology* **37**, 677–687 (1998). doi:10.1016/S0028-3908(98)00053-7 Medline

20. R. Biegler, R. G. Morris, Landmark stability: Further studies pointing to a role in spatial learning. *Q. J. Exp. Psychol. B* **49**, 307–345 (1996). Medline

21. J. M. Pearce, M. A. Good, P. M. Jones, A. McGregor, Transfer of spatial behavior between different environments: Implications for theories of spatial learning and for the role of the hippocampus in spatial learning. *J. Exp. Psychol. Anim. Behav. Process.* **30**, 135–147 (2004). doi:10.1037/0097-7403.30.2.135 Medline

22. P. M. Jones, J. M. Pearce, V. J. Davies, M. A. Good, A. McGregor, Impaired processing of local geometric features during navigation in a water maze following hippocampal lesions in rats. *Behav. Neurosci.* **121**, 1258–1271 (2007). doi:10.1037/0735-7044.121.6.1258 Medline

23. M. Stemmler, A. Mathis, A. V. M. Herz, Connecting multiple spatial scales to decode the population activity of grid cells. *Sci. Adv.* **1**, e1500816 (2015). doi:10.1126/science.1500816 Medline

24. C. Barry, C. Lever, R. Hayman, T. Hartley, S. Burton, J. O'Keefe, K. Jeffery, N. Burgess, The boundary vector cell model of place cell firing and spatial memory. *Rev. Neurosci.* **17**, 71–97 (2006). doi:10.1515/REVNEURO.2006.17.1-2.71 Medline

25. A. T. Keinath, R. A. Epstein, V. Balasubramanian, Environmental deformations dynamically shift the grid cell spatial metric. bioRxiv 174367 [Preprint]. 18 December 2017. https://doi.org/10.1101/174367

26. J. Koenig, A. N. Linder, J. K. Leutgeb, S. Leutgeb, The spatial periodicity of grid cells is not sustained during reduced theta oscillations. *Science* **332**, 592–595 (2011). doi:10.1126/science.1201685 Medline

27. M. P. Brandon, J. Koenig, J. K. Leutgeb, S. Leutgeb, New and distinct hippocampal place codes are generated in a new environment during septal inactivation. *Neuron* **82**, 789–796 (2014). doi:10.1016/j.neuron.2014.04.013 Medline

28. J. J. Jun, N. A. Steinmetz, J. H. Siegle, D. J. Denman, M. Bauza, B. Barbarits, A. K. Lee, C. A. Anastassiou, A. Andrei, Ç. Aydın, M. Barbic, T. J. Blanche, V. Bonin, J. Couto, B. Dutta, S. L. Gratiy, D. A. Gutnisky, M. Häusser, B. Karsh, P. Ledochowitsch, C. M. Lopez, C. Mitelut, S. Musa, M. Okun, M. Pachitariu, J. Putzeys, P. D. Rich, C. Rossant, W. L. Sun, K. Svoboda, M. Carandini, K. D. Harris, C. Koch, J. O'Keefe, T. D. Harris, Fully integrated silicon probes for high-density recording of neural activity. *Nature* **551**, 232–236 (2017). doi:10.1038/nature24636 Medline

29. C. Rossant, S. N. Kadir, D. F. M. Goodman, J. Schulman, M. L. D. Hunter, A. B. Saleem, A. Grosmark, M. Belluscio, G. H. Denfield, A. S. Ecker, A. S. Tolias, S. Solomon, G.

Buzsáki, M. Carandini, K. D. Harris, Spike sorting for large, dense electrode arrays. *Nat. Neurosci.* **19**, 634–641 (2016). doi:10.1038/nn.4268 Medline

30. M. Pachitariu, N. Steinmetz, S. Kadir, M. Carandini, K. D. Harris, Kilosort: Realtime spike-sorting for extracellular electrophysiology with hundreds of channels. bioRxiv 061481 [Preprint]. 30 June 2016. https://doi.org/10.1101/061481

31. https://github.com/kwikteam/phy.

32. M. A. Wilson, B. L. McNaughton, Dynamics of the hippocampal ensemble code for space. *Science* **261**, 1055–1058 (1993). doi:10.1126/science.8351520 Medline

33. K. Zhang, I. Ginzburg, B. L. McNaughton, T. J. Sejnowski, Interpreting neuronal population activity by reconstruction: Unified framework with application to hippocampal place cells. *J. Neurophysiol.* **79**, 1017–1044 (1998). doi:10.1152/jn.1998.79.2.1017 Medline